Remote Sensing Applications: Society and Environment 40 (2025) 101780

Contents lists available at ScienceDirect

Remote Sensing Applications: Society and Environment

journal homepage: www.elsevier.com/locate/rsase

Asymmetric and seasonal surface deformation of the Hoja-Mumin salt diapir, Tajikistan, revealed by an improved SBAS-InSAR method incorporating optimized interferogram selection

Yanqing Sun, Wenbin Xu *, Lei Xie, Zhidan Chen, Jiageng Wang, Baojun Shan

School of Geosciences and Info-Physics, Central South University, China

ARTICLE INFO

Keywords:
Hoja-Mumin
Salt diapirs
SBAS-InSAR
Surface deformation
Controlling factors

ABSTRACT

Salt diapirs, characterized by vertical deformation, host abundant natural resources and, owing to their complex deformation processes, significantly influence regional geological evolution and resource development. The Hoja-Mumin salt diapir, located in Tajikistan, is a typical piercement-type diapir whose deformation mechanisms remain largely unknown. This study uses an improved Small Baseline Subset Interferometric Synthetic Aperture Radar (SBAS-InSAR) method with optimized interferogram selection to monitor spatiotemporal surface deformation from October 2017 to December 2023. Interferometric pairs were selected based on visual phase-unwrapping quality, loop phase-closure consistency, and a coherence-variance assessment. The results reveal an asymmetric east–west deformation pattern, with maximum eastward and westward rates of approximately 26.8 cm/yr and 38.6 cm/yr, respectively. Vertical rates range from −17.4 cm/yr to 8.3 cm/yr. In addition to the long-term linear deformation, seasonal fluctuations were observed in the central zone. Topographic and climatic analyses suggest that eastward movement is impeded by inclined caprock, while both subsidence and horizontal deformation are positively correlated with local slope. Uplift is concentrated in the flatter central areas, and seasonal variations are strongly controlled by fluctuations in soil moisture and temperature in salt-bearing soils. The deformation of the salt diapir is jointly controlled by fault activity, gravity, topography, salt rheology, and regional climate. This study demonstrates the capability of InSAR to capture such complex deformation, elucidates the governing mechanisms, and provides a methodological reference for applying InSAR to salt diapir monitoring, resource development, and geological hazard assessment.

1. Introduction

Salt diapirs represent a unique type of vertical deformation structures (Edgell, 1996), with formation mechanisms that differ fundamentally from the predominantly horizontal movements observed in plate-tectonic settings (Dewey and Horsfield, 1970; Frisch et al., 2011). Salt diapir development is primarily driven by the buoyancy of low-density rock salt (Schultz-Ela, 2003). When overlain by denser strata, the system becomes gravitationally unstable. Once the buoyant force exceeds the strength of the overburden, the salt begins to rise, eventually forming a diapir that may reach the surface. Owing to its low porosity, low permeability, and high plasticity,

* Corresponding author.
E-mail address: wenbin.xu@csu.edu.cn (W. Xu).

https://doi.org/10.1016/j.rsase.2025.101780
Received 22 August 2025; Received in revised form 27 October 2025; Accepted 28 October 2025
Available online 28 October 2025

rock salt acts as an effective seal and caprock for hydrocarbons such as oil and natural gas (Hawkins and Moss, 2015). The formation and evolution of salt diapirs typically involve multiple driving mechanisms (Hassanpour et al., 2021). Monitoring and analyzing their deformation not only deepen our understanding of the underlying dynamics and controlling factors, but also provide a scientific foundation for resource exploration.

Deformation has been monitored with geodetic and remote sensing techniques, including leveling, Light Detection and Ranging (LiDAR), and the Global Navigation Satellite System (GNSS). However, their applications are often limited by restricted spatial coverage, insufficient accuracy, and dependence on observation conditions (Du et al., 2024). With the development of the Interferometric Synthetic Aperture Radar (InSAR) technique (Berardino et al., 2002; Hooper et al., 2004; Rosen et al., 1996), advantages such as wide spatial coverage, high precision, and all-weather, all-day monitoring have led to widespread applications in recent years in fields including earthquakes (Jiang et al., 2024), volcanology (Xu et al., 2015), and landslides (Luo et al., 2020). The technique has also proven valuable for monitoring the deformation of salt diapirs, which have complex geological structures (Manea et al., 2021; Shami et al., 2024). As early as 2006, InSAR was successfully applied to detect a maximum uplift rate of 8.3 mm/yr at the Mount Sedom salt diapir in the Dead Sea basin, revealing long-term and stable uplift in the region (Weinberger et al., 2006). In the Kuqa fold-thrust belt of northwestern China, InSAR delineated an asymmetric pattern of uplift and subsidence, which was likely influenced by local tectonic structures and topographic conditions (Colón et al., 2016). Roosta et al. (2019) applied the SBAS-InSAR technique to analyze the deformation of the Nasr-Abad salt diapir in Iran from 2003 to 2010. By integrating the InSAR time series with temperature and precipitation data, they identified distinct seasonal fluctuations. In summary, the InSAR technique, owing to its high precision and long-term monitoring capabilities, not only enables detailed measurements of surface deformation over salt diapirs, but also reveals the spatiotemporal evolution of deformation and the underlying controlling mechanisms. These insights contribute significantly to our understanding of the dynamic processes associated with salt tectonics.

The Hoja-Mumin salt diapir (37°44′N, 69°37′E) is located in Vose district of Khatlon Province, southern Tajikistan, and is a typical piercement-type diapir that exposes rock salt at the surface. Although significant surface deformation has been observed in this region, comprehensive studies of its deformation mechanisms remain limited. Notably, the region experiences significant seasonal climatic variations, making it an ideal natural laboratory for investigating deformation characteristics and their controlling factors.

This study aims to investigate the spatiotemporal evolution of surface deformation at the Hoja-Mumin salt diapir and to identify its primary controlling factors. An improved SBAS-InSAR approach with refined interferogram selection is applied to Sentinel-1A data from October 2017 to December 2023 on both ascending and descending tracks. Vertical and east–west displacement components are

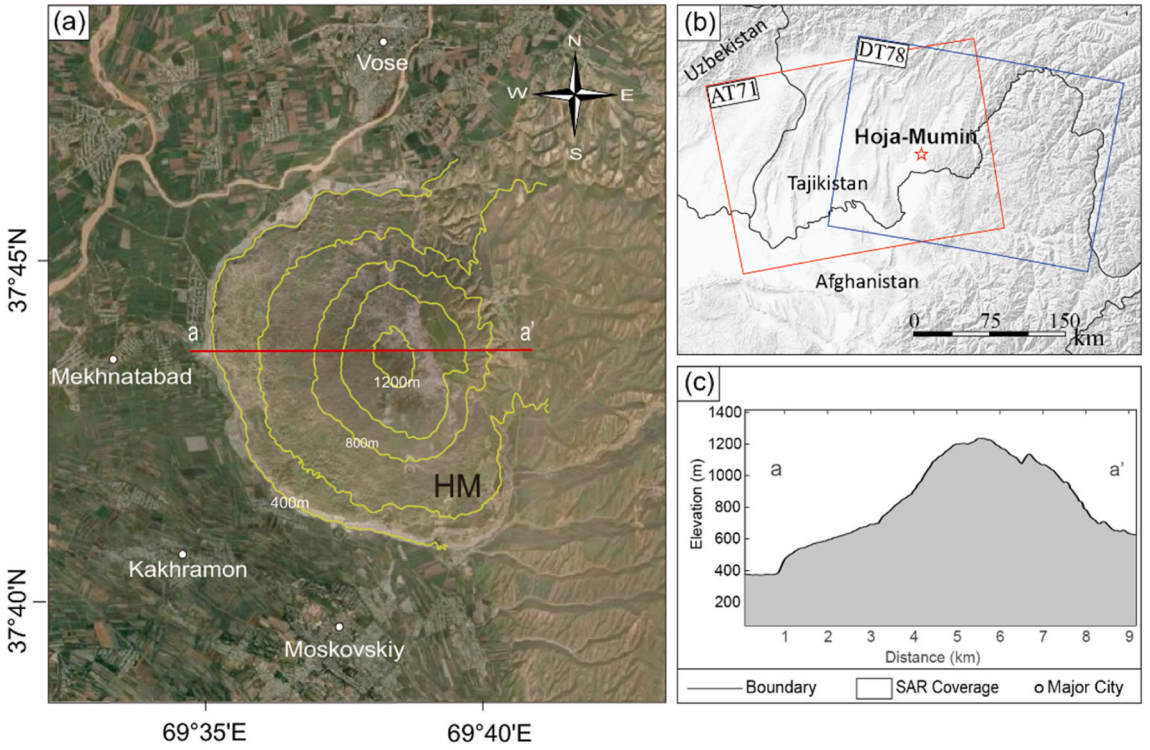

Fig. 1. (a) Optical imagery of the Hoja-Mumin salt diapir (Esri World Imagery). Yellow solid lines denote topographic contours delineating the primary salt diapir structure, with a 200 m interval. The red straight line indicates the selected profile line (aa'), and the white circles indicate the positions of major urban areas. (b) Spatial coverage of the Sentinel-1A SAR acquisitions used in this study. The red rectangle demarcates the ascending track coverage area, and the blue rectangle representing the descending track coverage. The location of the Hoja-Mumin salt diapir is marked by a red star. (c) Topographic elevation profile along the cross-section aa', with the cross-section location outlined in panel (a).

derived from the resulting line-of-sight (LOS) deformation maps. By analyzing the time-series deformation at representative points and the deformation-rate distributions along selected profiles, and by integrating temperature, precipitation, and geological data, we identify the key factors influencing the diapir's surface deformation. This study provides new insights into the deformation mechanisms and tectonic evolution of salt tectonics, thereby offering a valuable reference for understanding the dynamic interactions between salt-related deformation and external environmental factors.

2. Study area and datasets

2.1. Study area

The Hoja-Mumin salt diapir is one of the highest-elevation salt diapirs in the world. Its summit reaches an elevation of approximately 1330 m, standing about 860 m above the surrounding plain terrain. The diapir exhibits a prominent, massive structure with a surface area of approximately 55 km^2 (Fig. 1a and c). The Hoja-Mumin salt diapir is marked by a prominent dynamic bulge and is surrounded by distinctive geomorphological features, including numerous sinkholes, canyons, and fissures. Preliminary studies on the Hoja-Mumin salt diapir have already been conducted by several researchers. As early as 1986, Leith and Simpson noted that the Hoja-Mumin salt diapir shares certain similarities in activity and surrounding environment with the Kuh-e-Namak salt diapir in Iran (Talbot and Jarvis, 1984), and estimated its lateral expansion rate to be approximately 170 mm/yr (Leith and Simpson, 1986). The SBAS-InSAR technique was employed to derive the annual average displacement rates across the Tajik Basin and adjacent orogenic belts, revealing that the Hoja-Mumin salt diapir undergoes lateral expansion at a rate of less than 350 mm/yr (Metzger et al., 2021). Dooley et al. (2015) further demonstrated a tilted-roof-like barrier on the eastern flank of the Hoja-Mumin salt diapir, which impedes the eastward migration of the salt body. Their findings emphasized the significant role of tectonic activity in controlling the overall deformation pattern of the diapir. Additionally, Gągała et al. identified an active fault zone at depth in the region, through which salt continuously rises along fault planes and penetrates the overlying strata, resulting in notable surface displacement (Gągała et al., 2020).

In summary, although previous studies have preliminarily identified the surface deformation characteristics and some controls of the Hoja-Mumin salt diapir, systematic investigations of the spatiotemporal evolution and driving mechanisms of its deformation remain limited. Therefore, a comprehensive study of this salt diapir is essential for understanding the dynamics of salt tectonics, and it provides a valuable natural laboratory for exploring its controlling factors.

2.2. Datasets

The InSAR technique was employed to measure surface deformation at the Hoja-Mumin salt diapir. A total of 182 ascending-track and 181 descending-track Sentinel-1A Single Look Complex (SLC) images, provided by the European Space Agency (ESA) and acquired between October 2017 and December 2023 (Fig. 1b and Table 1), were used for interferometric processing. Additionally, a Digital Elevation Model (DEM) dataset covering the study region was used to remove the topographic phase component and to provide georeferenced coordinates (Farr and Kobrick, 2000; Farr et al., 2007). To minimize the impact of orbital errors on the accuracy of the results, Precise Orbit Determination (POD) data were also employed to support subsequent data processing.

To investigate the potential correlation between meteorological factors and surface deformation, monthly mean temperature and precipitation data from the Vose region, located ~4 km from the Hoja-Mumin salt diapir, were collected during the study period (Fig. 8a). Data were obtained from World Weather Online (https://www.worldweatheronline.com). The dataset shows strong seasonal variations, with precipitation concentrated in winter and spring, peaking around April, when monthly totals often exceed 100 mm, and this period coincides with lower temperatures. In contrast, precipitation drops sharply in summer and autumn, reaching near zero in July and August, reflecting a characteristic hot and arid climate. Overall, the climate of the Vose region exhibits a distinct seasonal cycle, alternating between cold, wet winter–spring and hot, dry summer–autumn conditions.

3. Methods

This study uses an improved SBAS-InSAR method with optimized interferogram selection to analyze the spatiotemporal evolution of surface deformation and the driving mechanisms at the Hoja-Mumin salt diapir (Fig. 2).

Table 1
Information on Sentinel-1A SAR acquisitions for ascending and descending orbits.

Parameters	Ascending orbit	Descending orbit
Frame ID	119	466
Path ID	71	78
Acquisition period (YYYYMM)	201710-202312	201710-202312
Number of scenes	182	181
Heading (°)	−13.3	193.3
Incidence (°)	39.5	39.5

3.1. Improved SBAS-InSAR data processing

Sentinel-1A SAR images were processed using the GAMMA software (Werner et al., 2000). A multi-master Small Baseline Subset InSAR (SBAS-InSAR) approach was adopted to achieve millimeter-scale deformation accuracy by constructing an interferogram network based on predefined temporal and spatial baseline thresholds (Berardino et al., 2002). Interferograms were multilooked with a ratio of 20 by 4 in the azimuth and range directions, respectively, to reduce noise and enhance coherence. The temporal and spatial baseline thresholds were set to 90 days and 100 m, respectively, with each scene allowed to form interferometric pairs with up to five other scenes. This configuration yielded 746 interferograms from ascending tracks and 759 from descending tracks. After network formation, differential interferograms were filtered and phase unwrapping was carried out using the Minimum Cost Flow (MCF) algorithm (Chen and Zebker, 2002; Goldstein and Werner, 1998). We manually checked and removed several interferograms that exhibited severe decorrelation and other quality issues to avoid significant phase-unwrapping errors that could consequently affect the accuracy of the subsequent deformation inversion.

Traditional interferometric approaches often suffer from decorrelation and phase noise over salt diapirs due to their complex surface conditions and temporal variability. To enhance the accuracy and stability of deformation monitoring, we employed a quality-driven interferogram selection strategy. After phase unwrapping, low-quality interferograms were excluded to reduce error propagation and improve the reliability of deformation estimates. The selection was optimized based on three criteria: visual inspection of unwrapping quality, loop phase closure consistency, and coherence variance. First, a manual visual inspection was conducted to examine each unwrapped interferogram, and those exhibiting global or localized unwrapping errors were removed. Second, phase closure consistency was assessed using a triangular closure method, in which triplets of interferograms form closed loops. In the absence of unwrapping errors, the loop phase should approach zero (Morishita et al., 2020). Accordingly, we computed the phase vector sum for each triangular closure; closures with errors larger than 1.5 rad were flagged, and interferograms repeatedly implicated in such closures were removed from further processing. Additionally, coherence variance was analyzed across all interferograms, and the top 10% with the highest variance were excluded to further enhance the reliability of deformation measurements. These optimization strategies effectively suppressed the impact of low-quality interferograms and increased the proportion of high-quality pairs in the subsequent inversion, thereby improving the overall accuracy of the deformation results. Consequently, three SAR scenes were removed from the ascending dataset, resulting in the elimination of 158 interferometric pairs, and four scenes were removed from the descending dataset, with 120 interferometric pairs discarded (Fig. 3).

3.2. Decomposition of LOS velocity into vertical and horizontal components

Because SAR operates in a side-looking geometry, InSAR typically measures only the LOS component of surface deformation. A

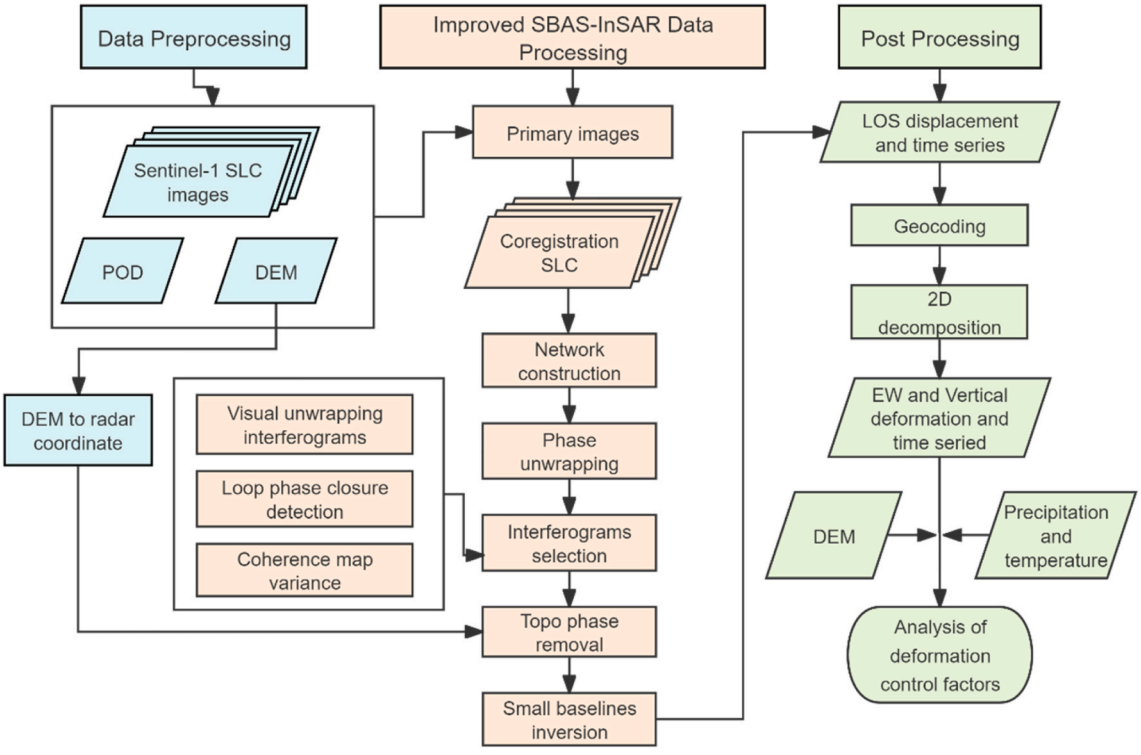

Fig. 2. Flowchart of the data processing.

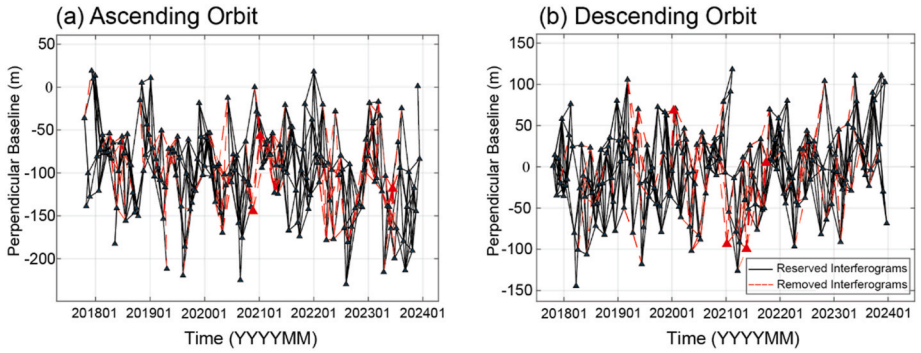

Fig. 3. Baseline-optimized SBAS-InSAR interferometric networks for (a) ascending and (b) descending tracks. In each panel, the horizontal axis corresponds to the acquisition time of Sentinel-1A SAR images, while the vertical axis denotes the perpendicular (spatial) baseline. Triangles represent individual SAR acquisitions, and connecting lines indicate interferometric pairs. Red markers highlight the SAR images and interferometric pairs excluded during baseline optimization and pair selection.

single LOS observation cannot recover the full three-dimensional motion; therefore, decomposition using multiple viewing geometries or auxiliary data is required. However, since the azimuth direction of the satellite is nearly parallel to the north–south direction, InSAR is weakly sensitive to north–south motion (Hanssen, 2001; Motagh et al., 2017). Therefore, this study neglects the north–south component, and the following equation is used to decompose the vertical and horizontal components from LOS displacements:

$$\begin{bmatrix} V_{Asc} \\ V_{Des} \end{bmatrix} = \begin{bmatrix} \cos\theta_{Asc} & -\sin\theta_{Asc}\sin(\alpha_{Asc} - 3\pi/2) \\ \cos\theta_{Des} & -\sin\theta_{Des}\sin(\alpha_{Des} - 3\pi/2) \end{bmatrix} \begin{bmatrix} V_U \\ V_E \end{bmatrix} \quad (1)$$

where V_{Asc} and V_{Des} represent LOS velocities in the ascending and descending directions, respectively; θ represents the incidence angle and α represents the azimuth angle; V_U and V_E correspond to the velocities in the up–down and east–west directions.

4. Results

4.1. InSAR LOS displacements

The LOS displacement fields over the Hoja-Mumin salt diapir are primarily concentrated on the western flank, revealing a marked asymmetry between ascending and descending track measurements. The western flank displays substantially greater deformation than the eastern flank (Fig. 4), with mean annual LOS rates of −23.3 cm/yr to 15.0 cm/yr (ascending) and −36.3 cm/yr to 11.8 cm/yr (descending). Moreover, comparative analysis of ascending and descending LOS deformation rates reveals opposite signs over most of the diapir structure, indicating that the LOS signal is dominated by the effects of horizontal motion parallel to the respective LOS directions (Fig. 4). The systematic discrepancies between ascending and descending track measurements underscore the necessity of multi-track dataset integration for a comprehensive analysis of surface deformation characteristics.

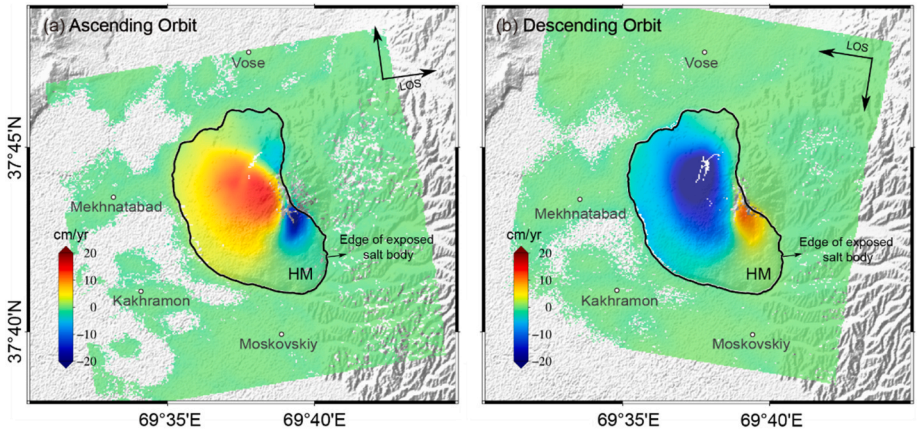

Fig. 4. Annual average LOS velocity derived from (a) ascending and (b) descending track time series. The black solid line outlines the edge of the exposed salt body. Major cities and regional locations within the study area are also labeled. HM: Hoja-Mumin salt diapir.

4.2. Vertical and horizontal displacements

By integrating the annual average LOS velocity fields from both ascending and descending tracks, and subsequently performing pixel-wise two-dimensional decomposition using Equation (1), the east–west and vertical displacement components across the Hoja-Mumin salt diapir were derived (Fig. 5). In the derived east–west deformation field, eastward displacement is defined as positive and westward displacement as negative, with deformation rates ranging from −38.6 cm/yr to 26.8 cm/yr, revealing a striking asymmetric pattern: the western flank demonstrates predominant westward movement while the eastern flank exhibits eastward motion. In the vertical field, uplift is defined as positive and subsidence as negative. The derived deformation rates range from −17.4 cm/yr to 8.3 cm/yr, revealing spatially heterogeneous vertical motions across the salt diapir. Distinct deformation patterns are observed: uplift dominates the central salt diapir area, while the surrounding regions generally exhibit subsidence, which appears to radiate outward from the uplifted core. Additionally, minor uplift is also observed in the southwestern and southern parts of the diapir.

To systematically investigate the two-dimensional deformation patterns of the Hoja-Mumin salt diapir, two representative cross-sectional profiles were selected within the study area to illustrate the spatial deformation distribution (Fig. 5a). Specifically, profile AA' transects the primary displacement field of the Hoja-Mumin salt diapir along a NW-SE orientation, while profile BB' provides complete coverage across the diapir structure along a SW-NE transect.

The analysis along profiles AA' and BB' across the Hoja-Mumin salt diapir reveals significant spatial variations in displacement and elevation patterns (Fig. 5). Along profile AA', maximum uplift reaches ~6 cm/yr, maximum subsidence reaches ~13 cm/yr, westward displacement reaches ~40 cm/yr, and the maximum eastward displacement reaches ~25 cm/yr. Along profile BB', the maximum uplift and subsidence rates are ~6 cm/yr and ~4 cm/yr, respectively; maximum westward displacement reaches 35 cm/yr, while eastward displacement is minimal and can be neglected. The spatial distribution of deformation rates reveals that the east–west deformation is primarily concentrated on either side of the salt diapir, with a broader western displacement zone. Uplift deformation is mainly confined to the summit of the salt diapir where elevations exceed 1100 m, while subsidence is predominantly distributed around the uplift zone and extends outward. In addition, areas with steep slopes at elevations around 1000 m exhibit relatively high subsidence and horizontal displacement rates, indicating a strong correlation between topography and surface displacement.

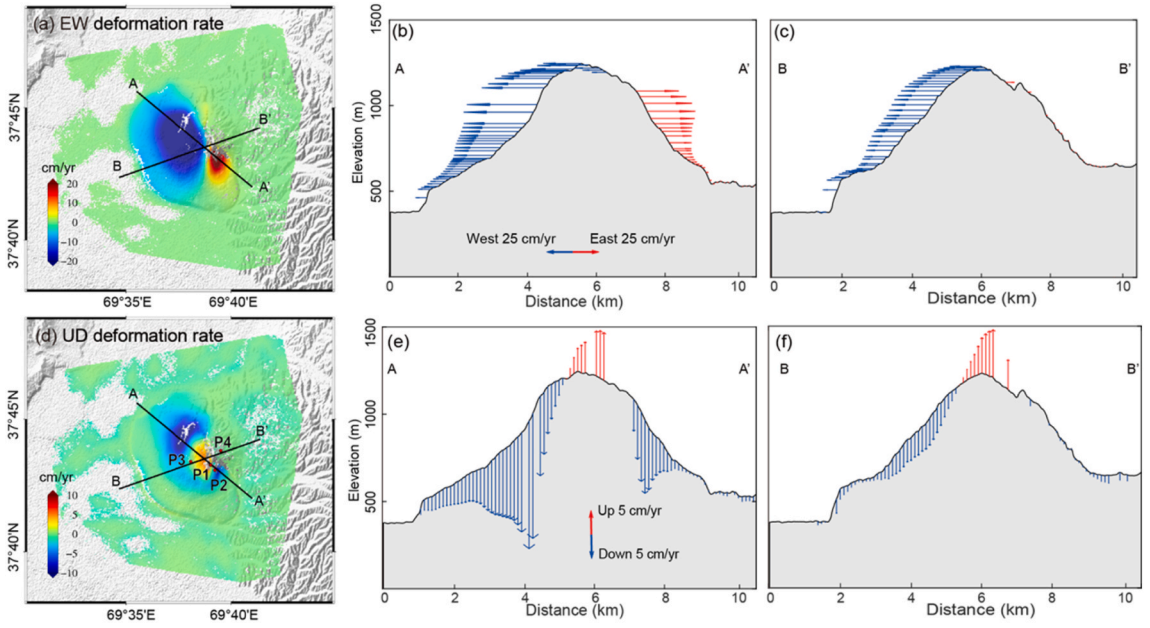

Fig. 5. Two-dimensional deformation field and cross-sectional velocity profiles of the Hoja-Mumin salt diapir. (a) Mean annual east–west deformation velocity field. Two representative cross-section lines (AA' and BB') are selected for further analysis. (b) East–west deformation velocity profile along AA'. Arrows denote both direction and magnitude of horizontal displacement, with blue and red vectors indicating westward and eastward motion, respectively. Vector length scales linearly with deformation rate. (c) East–west deformation velocity profile along BB'. (d) Mean annual vertical deformation velocity field. Points P1–P4, located around the uplift zone, are selected as representative sites for time-series deformation analysis. (e) Vertical deformation velocity profile along AA'. Arrows represent direction and magnitude of vertical displacement, where blue and red vectors correspond to subsidence and uplift, respectively. Vector length is proportional to displacement rate. (f) Vertical deformation velocity profile along BB'.

5. Discussions

5.1. Correlation between salt diapir topographic slope and surface deformation

The spatial distribution of vertical deformation over the Hoja-Mumin salt diapir, in relation to terrain slope, exhibits notable patterns including summit uplift, flank subsidence along the NW-SE orientation, and localized uplift near the base of the slopes. The uplift zone of the Hoja-Mumin salt diapir is located at its summit, where the terrain is relatively gentle, with slopes generally less than 10°. In contrast, the adjacent subsidence regions exhibit higher rates, which are commonly associated with steeper slopes. As shown in the spatial distribution of vertical deformation rates and slope gradients (Fig. 6), T2 and T4, which exhibit relatively steep slopes, also experience high subsidence rates. In contrast, T3, which undergoes significant uplift, is located in an area with gentle terrain (slope <5°). These results indicate a positive correlation between slope steepness and the rate of subsidence, whereas no clear relationship is observed between uplift deformation and slope gradient. Furthermore, the distribution of east–west deformation rates along the cross-sectional profiles (Fig. 5b–c) reveals a clear positive correlation between slope gradient and horizontal deformation rates. The dissolution and lateral flow of halite reduce the structural support beneath the overlying strata, leading to both subsidence and outward extension toward the flanks. A positive correlation is observed between topographic slope and deformation rate, with steeper slopes exhibiting more distinct deformation.

In the southwestern and southern marginal zones of the salt diapir, where the terrain is relatively gentle with slopes generally less than 10°, the vertical surface deformation exhibits slight uplift. This uplift manifests as a spatial transition in which deformation evolves from a summit-fringing subsidence zone, diminishes outward, and eventually gives way to uplift. The progressively decreasing slope in this area limits the mobility of surface materials, leading to material accumulation and deposition. On the one hand, the decreasing slope weakens the gravity-driven subsidence rate; on the other hand, the continuous accumulation of surface material increases the surface load. When the rate of surface subsidence falls below that of material deposition, the dominance of deposition is manifested in InSAR observations as a slight uplift. This spatial transition from subsidence to uplift highlights that vertical deformation in this area is not only governed by gravity-related mechanisms modulated by topographic gradients, but also influenced by surface material accumulation, reflecting the combined effects of both processes.

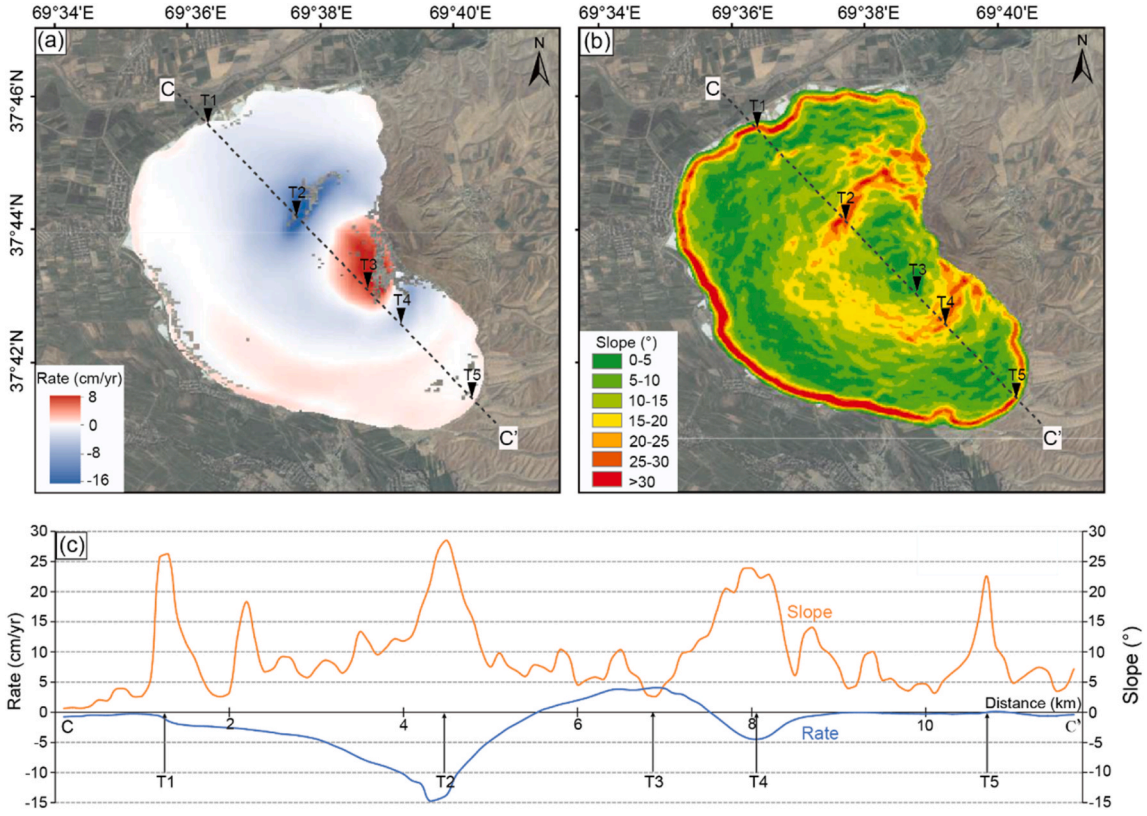

Fig. 6. Vertical deformation characteristics and slope analysis of the Hoja-Mumin salt diapir. (a) Annual average vertical deformation velocity in the Hoja-Mumin salt diapir. The representative profile line CC' is indicated, and points T2, T3, and T4 denote locations of significant uplift or subsidence. (b) Slope distribution map of the salt diapir. Points T1 and T5 correspond to areas with relatively steep terrain. (c) Variations in vertical deformation velocity and slope along CC' profile line.

5.2. Correlation between salt diapir structure and surface deformation

The Hoja-Mumin salt diapir exhibits pronounced east–west asymmetry in horizontal deformation. The overall deformation pattern is characterized by dominant westward motion, with the western sector displaying larger deformation magnitudes and a broader spatial extent. In contrast, the eastern sector displays significantly weaker deformation, with clear signs of impeded movement (Fig. 5a). This asymmetric distribution of horizontal deformation is likely associated with the internal structural features of the salt diapir. A prominent geomorphological boundary is clearly observed at the interface between the eastern and western deformation zones (Fig. 7). This boundary separates distinct geological and geomorphological units on either side and aligns closely with the transition in horizontal deformation patterns. Around the actively uplifting core of the diapir, the salt body flows outward in all directions, indicating a radial expansion trend. However, a tilted "roof-shaped structure" in the eastern part of the diapir acts as a physical barrier (Schultz-Ela et al., 1993). This inclined cap-like structure alters the local stress field and redirects salt flow pathways (Dooley et al., 2015), effectively restricting eastward propagation and lateral extrusion of the salt. As a result, horizontal deformation is predominantly concentrated on the western flank of the diapir, resulting in the observed asymmetric deformation pattern.

According to the contact relationships between salt bodies and surrounding strata, salt tectonics are generally classified into two types: piercing and non-piercing salt structures (Brandes et al., 2013). Piercing structures involve salt bodies that breach the overburden or come into contact with the surrounding rocks through faulting, while non-piercing salt structures refer to cases where the salt body does not directly penetrate the overlying strata. Once a salt body rises to a critical elevation, the underlying salt conduit may become unstable due to its inability to support the weight of the overlying mass (Hudec and Jackson, 2007). Under gravitational forces, this instability can trigger the formation of a viscous salt fountain, whereby salt extrudes onto the surface and accumulates as a flow-like deposit (Jackson and Talbot, 1986). The Hoja-Mumin salt diapir is a typical example of a piercing-type diapiric structure. It is situated in the transitional zone between the basin and the surrounding mountainous region, where topographic relief is highly variable and fault activity is frequent. These active faults provide favorable channels for the upward migration and piercing of salt bodies (Gągała et al., 2020). Under long-term tectonic stress, halite exhibits pronounced plasticity and low density, along with strong flowability. Driven by a combination of buoyant forces and compressive stress, the salt body ascends along fault planes, penetrating the overlying strata and eventually reaching the surface. Once extruded, gravitational forces shape the salt into banded or diapir-like surface structures known as salt diapirs (Santolaria et al., 2021). If the salt supply rate from the subsurface source exceeds the rate of surface lateral diffusion, continuous replenishment of salt material occurs at the outcrop, resulting in notable surface uplift. This also indicates that the salt source beneath the Hoja-Mumin salt diapir remains active. Overall, the deformation of the Hoja-Mumin salt diapir is primarily controlled by the rheological behavior of halite, buoyancy-driven flow, and the activity of fault structures, which together shape the morphology and long-term evolution of the salt diapir.

5.3. Coupling of periodic deformation of salt diapir with climate change

To investigate the seasonal effects of surface deformation over the Hoja-Mumin salt diapir, four representative points (P1, P2, P3, and P4) surrounding the uplift zone were selected (Fig. 5d): P1 is located within the maximum uplift sector, P2 lies in an area of significant subsidence, whereas P3 and P4 are situated in relatively stable areas surrounding the uplift zone, and their vertical time-

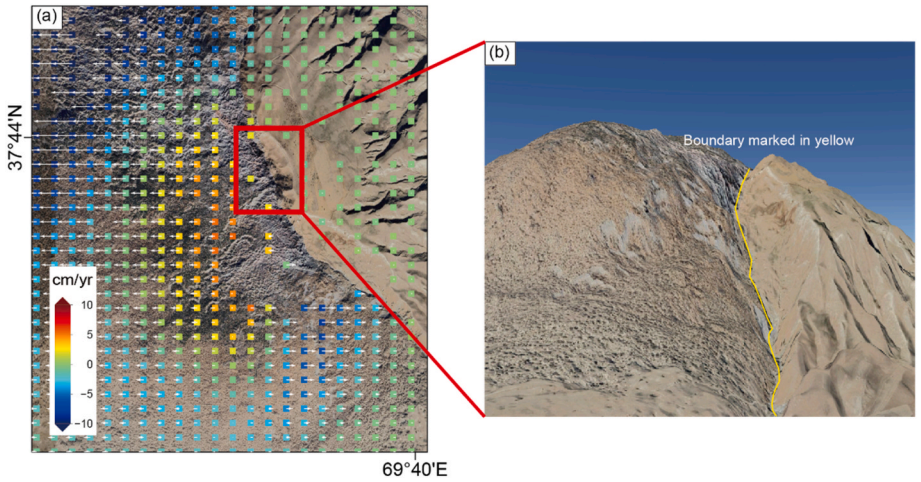

Fig. 7. (a) Integrated vertical and horizontal deformation fields across the uplift zone of the Hoja-Mumin salt diapir, overlaid on optical imagery. Color-coded squares represent vertical deformation rates (cm/yr), with warm and cool colors representing uplift and subsidence, respectively. Displacement vectors (arrows) depict both orientation and relative magnitude of horizontal deformation, where vector length scales proportionally with displacement rate. The red rectangle outlines a sector exhibiting a distinct geomorphological boundary. (b) Perspective view of the area delineated in panel (a), where yellow solid lines indicate manually interpreted geomorphic boundaries derived from surface texture and deformation pattern recognition.

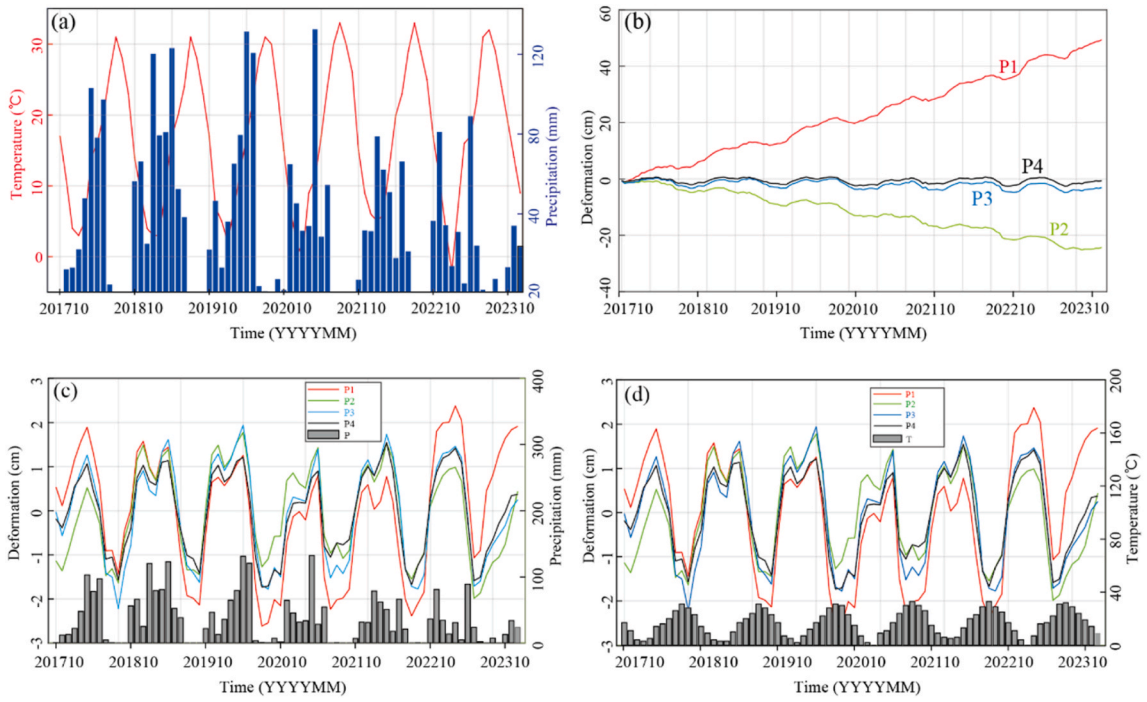

Fig. 8. (a) Monthly mean precipitation and temperature in the Vose region of Tajikistan from October 2017 to December 2023. (b) Vertical displacement time series at four representative points (P1–P4). (c) Residual (nonlinear) vertical deformation components and corresponding precipitation records at the four points. Solid lines depict deformation difference series, while vertical bars represent monthly precipitation totals. (d) Residual (nonlinear) vertical deformation components and associated temperature data. Solid lines indicate deformation difference series, and vertical bars display monthly-mean temperature.

series deformation curves were plotted (Fig. 8b). The results show that only P1 exhibits uplift, with a cumulative vertical displacement of nearly 50 cm; in contrast, P2, P3, and P4 display subsidence, with P2 showing the largest subsidence of approximately 25 cm. All four points exhibit similar periodic fluctuations, indicating a strong seasonal deformation pattern. To extract the seasonal deformation component and further investigate periodic characteristics, we fitted linear trends to the displacement time series at the four representative points. The residuals from these fits were taken as the nonlinear component used to characterize periodic variability. Positive residuals indicate relative uplift, whereas negative residuals indicate relative subsidence. These residual time series were then analyzed in conjunction with local precipitation and temperature records (Fig. 8c and d). The results indicate that surface deformation at the Hoja-Mumin salt diapir is characterized by a superposition of a long-term linear trend and seasonal fluctuations, with an amplitude of approximately 2 cm. A notable increase in subsidence is observed from June to October each year, followed by a slight uplift from October to the following June. Additionally, the residual deformation exhibits a moderate positive correlation with precipitation and a negative correlation with temperature, suggesting that seasonal climatic factors may influence the observed deformation patterns.

To further quantify the correlation characteristics, the Pearson correlation coefficient was employed as a statistical metric to assess the strength and direction of the linear relationship between two continuous variables. This coefficient ranges from −1 to 1: values close to 1 indicate a strong positive correlation, values near −1 indicate a strong negative correlation, and values around 0 suggest no significant linear relationship (Buytaert et al., 2006). Pearson correlation coefficients were then calculated between the residual vertical-displacement time series at the four characteristic points and the corresponding precipitation and temperature data to assess the relationship between surface deformation and climatic factors. The results show that the correlation coefficients between deformation and precipitation are 0.48, 0.63, 0.64, and 0.59 (P1−P4), indicating a moderate positive correlation. This suggests that increased precipitation is associated with uplift. In contrast, the correlation coefficients with temperature are −0.69, −0.73, −0.75, and −0.79 (P1−P4), indicating a strong negative correlation. This implies that during hotter and drier periods, slight surface subsidence may occur.

Seasonal climatic factors such as precipitation and temperature play a critical role in the time series of displacement (Champagnac et al., 2012; Roosta et al., 2019). The surface deformation of the Hoja-Mumin salt diapir is influenced by both the properties of the local evaporite materials and the regional climatic conditions, and exhibits significant seasonal variability. During winter and spring, low temperatures and abundant precipitation markedly increase soil moisture content. The absorption of water by rock salt causes volumetric expansion and produces a short-term “supporting effect”, manifested as slight surface uplift. Subsequently, the dissolution of salt minerals reduces interparticle friction and weakens soil strength, leading to a gradual attenuation of uplift (Wang et al., 2007). Under the combined influence of self-weight and external loading, the uplift further diminishes and may eventually transition into

subsidence (Wang et al., 2016). In contrast, during summer and autumn, high temperatures and reduced precipitation cause moisture loss from the shallow soil layers, resulting in pore compaction and minor surface subsidence. Subsequently, elevated surface temperatures induce thermal expansion of both rock salt and the surrounding strata, partially counteracting the subsidence. Overall, the seasonal deformation pattern of the Hoja-Mumin salt diapir is driven by the coupled effects of moisture variation and temperature in the shallow salt-bearing soils: the cold, wet seasons are dominated by water absorption and dissolution processes, during which uplift gradually weakens; the hot, dry seasons are characterized by drying-induced contraction, moderated by subsequent thermal expansion.

6. Conclusions

The study employed an improved SBAS-InSAR method with enhanced interferogram selection criteria to investigate surface deformation of the Hoja-Mumin salt diapir from October 2017 to December 2023. The spatiotemporal characteristics of deformation and its controlling factors were systematically analyzed. The results reveal a marked asymmetry in east–west horizontal deformation, with eastward motion notably constrained in the eastern sector. Vertical deformation displays a diapir-shaped pattern, characterized by uplift at the summit and subsidence along the flanks. The maximum eastward rate reaches approximately 26.8 cm/yr, whereas the westward rate is as high as ~38.6 cm/yr. Concurrent uplift and subsidence are observed, with maximum rates of about 8.3 cm/yr and 17.4 cm/yr, respectively. A comprehensive analysis integrating topographic and climatic data indicates that continuous uplift occurs in the gently sloping central area of the diapir, suggesting the presence of an active salt supply. Subsidence and horizontal deformation rates are positively correlated with local slope gradients, implying a significant topographic constraint on deformation. In addition, coupled variations in soil moisture and temperature across the region induce minor periodic deformation fluctuations around the uplift zones of the salt diapir, demonstrating the high effectiveness of InSAR in characterizing surface deformation patterns and elucidating their underlying mechanisms.

CRediT authorship contribution statement

Yanqing Sun: Data curation, Formal analysis, Methodology, Software, Visualization, Writing – original draft, Writing – review & editing. **Wenbin Xu:** Funding acquisition, Methodology, Project administration, Supervision, Writing – review & editing. **Lei Xie:** Methodology, Writing – review & editing. **Zhidan Chen:** Methodology, Visualization, Writing – review & editing. **Jiageng Wang:** Formal analysis, Methodology, Writing – review & editing. **Baojun Shan:** Methodology, Writing – review & editing.

Ethical statement

The authors declare that this research did not involve human participants, animals, or any experiments requiring ethical approval.

Declaration of competing interest

The authors declare that they have no known competing financial interests or personal relationships that could have appeared to influence the work reported in this paper.

Acknowledgements

This research is supported by the Natural Science Foundation of Hunan Province (2024JJ3031), National Natural Science Foundation of China (42174023, 42304037), Frontier Cross Research Project of Central South University (2023QYJC006).

Data availability

The authors do not have permission to share data.

References

Berardino, P., Fornaro, G., Lanari, R., Sansosti, E., 2002. A new algorithm for surface deformation monitoring based on small baseline differential SAR interferograms. IEEE Trans. Geosci. Rem. Sens. 40, 2375–2383.

Brandes, C., Schmidt, C., Tanner, D.C., Winsemann, J., 2013. Paleostress pattern and salt tectonics within a developing foreland basin (north-western subhercynian basin, northern Germany). Int. J. Earth Sci. 102, 2239–2254.

Buytaert, W., Celleri, R., Willems, P., Bièvre, B.D., Wyseure, G., 2006. Spatial and temporal rainfall variability in mountainous areas: a case study from the south ecuadorian andes. J. Hydrol. 329, 413–421.

Champagnac, J.-D., Molnar, P., Sue, C., Herman, F., 2012. Tectonics, climate, and mountain topography. J. Geophys. Res. Solid Earth 117, B02403.

Chen, C.W., Zebker, H.A., 2002. Phase unwrapping for large SAR interferograms: statistical segmentation and generalized network models. IEEE Trans. Geosci. Rem. Sens. 40, 1709–1719.

Colón, C., Webb, A.A.G., Lasserre, C., Doin, M.-P., Renard, F., Lohman, R., Li, J., Baudoin, P.F., 2016. The variety of subaerial active salt deformations in the kuqa fold-thrust belt (China) constrained by InSAR. Earth Planet Sci. Lett. 450, 83–95.

Dewey, J.F., Horsfield, B., 1970. Plate tectonics, Orogeny and Continental growth. Nature 225, 521–525.

Dooley, T.P., Jackson, M.P.A., Hudec, M.R., 2015. Breakout of squeezed stocks: dispersal of roof fragments, source of extrusive salt and interaction with regional thrust faults. Basin Res. 27, 3–25.

Du, J., Li, Z., Song, C., Zhu, W., Tomás, R., 2024. Coupling effect of impoundment and irrigation on landslide movement in maoergai reservoir area revealed by multi-platform InSAR observations. Int. J. Appl. Earth Obs. Geoinf. 129, 103802.
Edgell, H.S., 1996. Salt Tectonism in the Persian Gulf Basin, vol 100. Geological Society, London, Special Publications, pp. 129–151.
Farr, T.G., Kobrick, M., 2000. Shuttle radar topography mission produces a wealth of data. Trans. Am. Geophys. Union 81, 583–585.
Farr, T.G., Rosen, P.A., Caro, E., Crippen, R., Duren, R., Hensley, S., Kobrick, M., Paller, M., Rodriguez, E., Roth, L., Seal, D., Shaffer, S., Shimada, J., Umland, J., Werner, M., Oskin, M., Burbank, D., Alsdorf, D., 2007. The shuttle radar topography mission. Rev. Geophys. 45, RG2004.
Frisch, W., Meschede, M., Blakey, R., 2011. Plate Tectonics: Continental Drift and Mountain Building.
Gągała, Ł., Ratschbacher, L., Ringenbach, J.-C., Kufner, S.-K., Schurr, B., Dedow, R., Abdulhameed, S., Le Garzic, E., Gadoev, M., Oimahmadov, I., 2020. Tajik basin and Southwestern tian Shan, northwestern India-Asia collision zone: 1. Structure, kinematics, and salt tectonics in the Tajik fold-and-thrust belt of the Western foreland of the Pamir. Tectonics 39, e2019TC005871.
Goldstein, R.M., Werner, C.L., 1998. Radar interferogram filtering for geophysical applications. Geophys. Res. Lett. 25, 4035–4038.
Hanssen, R.F., 2001. Radar interferometry data interpretation and error analysis. Radar Interferometry Data Interpretation and Error Analysis.
Hassanpour, J., Muñoz, J.A., Yassaghi, A., Ferrer, O., Jahani, S., Santolaria, P., SeyedAli, S.M., 2021. Impact of salt layers interaction on the salt flow kinematics and diapirism in the eastern Persian gulf, Iran: constraints from seismic interpretation, sequential restoration, and physical modelling. Tectonophysics 811, 228887.
Hawkins, D., Moss, J., 2015. Economic impact of a salt dome natural gas storage facility. J. Econ. Dev. Stud. 3, 1–9.
Hooper, A., Zebker, H., Segall, P., Kampes, B., 2004. A new method for measuring deformation on volcanoes and other natural terrains using InSAR persistent scatterers. Geophys. Res. Lett. 31.
Hudec, M.R., Jackson, M.P.A., 2007. Terra infirma: understanding salt tectonics. Earth Sci. Rev. 82, 1–28.
Jackson, M.P.A., Talbot, C.J., 1986. External shapes, strain rates, and dynamics of salt structures. Geol. Soc. Am. Bull. 97, 305–323.
Jiang, K., Xu, W., Xie, L., 2024. Unwrap intractable C-Band coseismic interferograms: an improved SNAPHU method with range offset gradients as prior information. J. Geophys. Res. Solid Earth 129, e2024JB028826.
Leith, W., Simpson, D.W., 1986. Earthquakes related to active salt doming near kulyab, tadjikistan, USSR. Geophys. Res. Lett. 13, 1019–1022.
Luo, X., Wang, C., Long, Y., Yi, Z., 2020. Analysis of the decadal kinematic characteristics of the daguangbao landslide using multiplatform time series InSAR observations after the wenchuan earthquake. J. Geophys. Res. Solid Earth 125, e2019JB019325.
Manea, V.C., Armas, I., Manea, M., Gheorghe, M., 2021. InSAR surface deformation and numeric modeling unravel an active salt diapir in southern Romania. Sci. Rep. 11, 12091.
Metzger, S., Gągała, Ł., Ratschbacher, L., Lazecký, M., Maghsoudi, Y., Schurr, B., 2021. Tajik depression and greater Pamir neotectonics from InSAR rate maps. J. Geophys. Res. Solid Earth 126, e2021JB022775.
Morishita, Y., Lazecky, M., Wright, T.J., Weiss, J.R., Elliott, J.R., Hooper, A., 2020. LiCSBAS: an open-source InSAR time series analysis package integrated with the LiCSAR automated Sentinel-1 InSAR processor. Remote Sens. 12, 424.
Motagh, M., Shamshiri, R., Haghshenas Haghighi, M., Wetzel, H.-U., Akbari, B., Nahavandchi, H., Roessner, S., Arabi, S., 2017. Quantifying groundwater exploitation induced subsidence in the rafsanjan plain, southeastern Iran, using InSAR time-series and in situ measurements. Eng. Geol. 218, 134–151.
Roosta, H., Jalalifar, H., Nasab, S.K., Ranjbar, M., 2019. Seven years of surface deformation above the buried nasr-abad salt diapir using InSAR time-series analysis, central Iran. J. Geodyn. 130, 1–11.
Rosen, P.A., Hensley, S., Zebker, H.A., Webb, F.H., Fielding, E.J., 1996. Surface deformation and coherence measurements of Kilauea volcano, Hawaii, from SIR-C radar interferometry. J. Geophys. Res.-Planets 101, 23109–23125.
Santolaria, P., Ferrer, O., Rowan, M.G., Snidero, M., Carrera, N., Granado, P., Muñoz, J.A., Roca, E., Schneider, C.L., Piña, A., Zamora, G., 2021. Influence of preexisting salt diapirs during thrust wedge evolution and secondary welding: insights from analog modeling. J. Struct. Geol. 149, 104374.
Schultz-Ela, D.D., 2003. Origin of drag folds bordering salt diapirs. AAPG (Am. Assoc. Pet. Geol.) Bull. 87, 757–780.
Schultz-Ela, D.D., Jackson, M.P.A., Vendeville, B.C., 1993. Mechanics of active salt diapirism. Tectonophysics 228, 275–312.
Shami, S., Shahriari, M.A., Nilfouroushan, F., Forghani, N., Salimi, M., Reshadi, M.A.M., 2024. Surface displacement measurement and modeling of the shah-gheyb salt dome in southern Iran using InSAR and machine learning techniques. Int. J. Appl. Earth Obs. Geoinf. 132, 104016.
Talbot, C.J., Jarvis, R.J., 1984. Age, budget and dynamics of an active salt extrusion in Iran. J. Struct. Geol. 6, 521–533.
Wang, C., Jiang, C., Xie, Q., Feng, T., 2007. Change in microstructure of salty soil during crystallization. J. Southwest Jiaot. Univ. 20, 66–69.
Wang, D., Liu, J., Li, X., 2016. Numerical simulation of coupled water and salt transfer in soil and a case study of the expansion of subgrade composed by saline soil. Procedia Eng. 143, 315–322.
Weinberger, R., Begin, Z.B., Waldmann, N., Gardosh, M., Baer, G., Frumkin, A., Wdowinski, S., 2006. Quaternary rise of the sedom diapir, dead sea basin. In: Enzel, Y., Agnon, A., Stein, M. (Eds.), New Frontiers in Dead Sea Paleoenvironmental Research. Geological Society of America, pp. 1–401.
Werner, C.L., Wegmüller, U., Strozzi, T., Wiesmann, A., 2000. Gamma SAR and interferometric processing software. In: Proceedings of the ers-envisat Symposium, Gothenburg, Sweden. Proceedings of the ers-envisat Symposium, pp. 1–1620. Gothenburg, Sweden.
Xu, W., Ruch, J., Jónsson, S., 2015. Birth of two volcanic islands in the southern Red Sea. Nat. Commun. 6, 7104.